minerals

MDPI

Article

Zircon Macrocrysts from the Drybones Bay Kimberlite Pipe (Northwest Territories, Canada): A High-Resolution Trace Element and Geochronological Study

Ekaterina P. Reguir [1,*], Anton R. Chakhmouradian [1], Barrett Elliott [2], Ankar R. Sheng [1] and Panseok Yang [1]

[1] Department of Geological Sciences, University of Manitoba, 125 Dysart Road, Winnipeg, MB R3T 2N2, Canada; chakhmou@cc.umanitoba.ca (A.R.C.); mr.ankar@gmail.com (A.R.S.); Panseok.Yang@umanitoba.ca (P.Y.)

[2] Northwest Territories Geological Survey, 4601-B 52 Avenue, Yellowknife, NT X1A 1K3, Canada; Barrett_Elliott@gov.nt.ca

* Correspondence: umreguir@cc.umanitoba.ca; Tel.: +1-204-474-8765

Received: 1 October 2018; Accepted: 22 October 2018; Published: 25 October 2018

Abstract: Zircon macrocrysts in (sub)volcanic silica-undersaturated rocks are an important source of information about mantle processes and their relative timing with respect to magmatism. The present work describes variations in trace element (Sc, Ti, Y, Nb, lanthanides, Hf, Ta, Pb, Th, and U) and isotopic (U-Pb) composition of zircon from the Drybones Bay kimberlite, Northwest Territories, Canada. These data were acquired at a spatial resolution of ≤100 μm and correlated to the internal characteristics of macrocrysts (imaged using cathodoluminescence, CL). Six types of zircon were distinguished on the basis of its luminescence characteristics, with the majority of grains exhibiting more than one type of CL response. The oscillatory-zoned core and growth sectors of Drybones Bay zircon show consistent variations in rare-earth elements (REE), Hf, Th, and U. Their chondrite-normalized REE patterns are typical of macrocrystic zircon and exhibit extreme enrichment in heavy lanthanides and a positive Ce anomaly. Their Ti content decreases slightly from the core into growth sectors, but the Ti-in-zircon thermometry gives overlapping average crystallization temperatures (820 ± 26 °C to 781 ± 19 °C, respectively). There is no trace element or CL evidence for Pb loss or other forms of chemical re-equilibration. All distinct zircon types are concordant and give a U-Pb age of 445.6 ± 0.8 Ma. We interpret the examined macrocrysts as products of interaction between a shallow (<100 km) mantle source and transient kimberlitic melt.

Keywords: zircon; macrocrysts; kimberlite; trace elements; geochronology; cathodoluminescence; Ti-in-zircon geothermometry

1. Introduction

The Slave craton in northern Canada is a small (~200,000 km^2) but well-exposed fragment of Archean (4.05–2.55 Ga) continental crust that hosts a variety of gold, silver, base metal, critical metal, and gemstone deposits. Notably, the latter include >300 kimberlite bodies (vents, dikes, and diatremes) [1]. The discovery of first diamondiferous kimberlites in the Lac de Gras area in 1991 sparked the largest claim-staking rush in Canadian mining history [2], which ultimately paved the way to the development of five new mines to date (Ekati since 1998, Diavik since 2003, Jericho in 2006–2008, Snap Lake in 2008–2015, and Gahcho Kué since 2016). Nineteen individual bodies have been, or are presently, mined and about a dozen other kimberlite clusters are under active exploration (Figure 1).

An increase in diamond production in recent years has moved Canada up to the second place in the global market in volume terms (23.2 million carats valued at $2.06 billion in 2017).

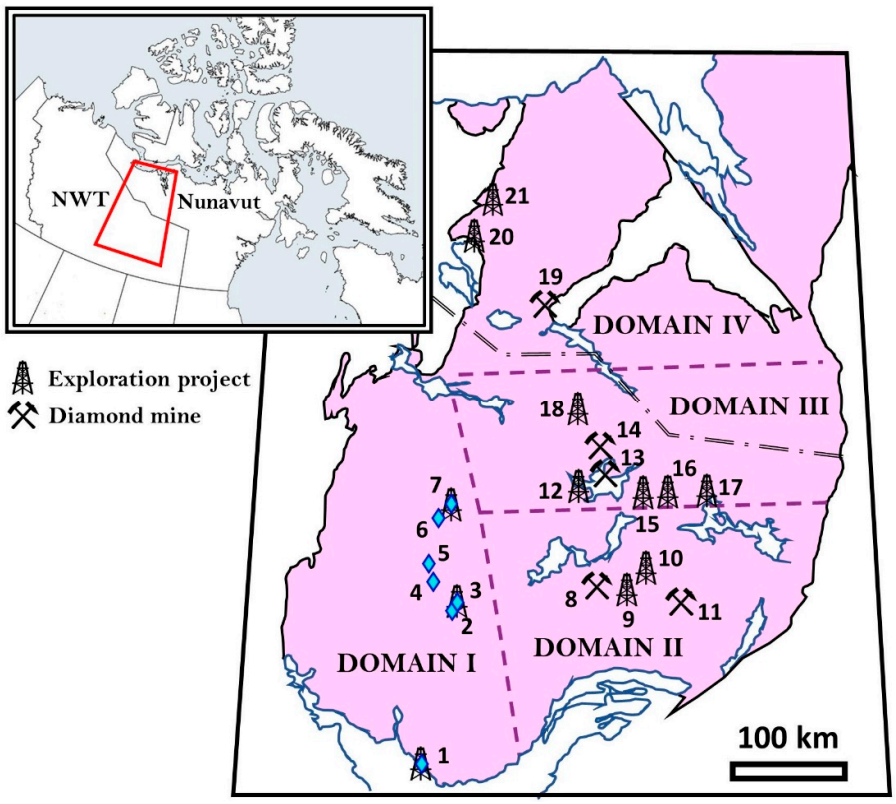

Figure 1. Schematic location map (outlined red in the inset) of the four major kimberlite domains in the Archean Slave craton (pink); based on Heaman et al. (2003), NWT Government (2016) and an unpublished kimberlite database (NWT Geological Survey). Siluro-Ordovician kimberlites are indicated by blue diamonds and include: (1) Drybones Bay and Mud Lake; (2) Ursa and Winny; (3) Orion and Cross; (4) Jean, Cirque, and Rich; (5) Willow; (6) Kent, Otter, PCE, Wolverine North, and South; (7) Aquila and Cygnus. Other localities: (8) Snap Lake mine; (9) Camsel Lake; (10) Munn Lake; (11) Gahcho Kué mine; (12) Monument Bay; (13) Diavik mine; (14) Ekati mine; (15) DO27; (16) Afridi Lake; (17) Nicholas Bay; (18) Yamba Lake; (19) Jericho mine; (20) Anuri; (21) Hammer. NWT–Nunavut territorial boundary is marked by a black dot-dashed line. NWT: Northwest Territories.

Only a small number of the 300-plus Slave kimberlites have been studied in significant detail. As can be expected, the bulk of published work is focused on the producing areas, especially the Ekati and Diavik mines at Lac de Gras. One of the least-studied areas with a poorly understood potential is the southwestern section of the craton hosting Early- to Mid-Paleozoic kimberlites, which are aligned in a roughly longitudinal fashion from Drybones Bay and Mud Lake along the northern shore Great Slave Lake to the Aquila and Cygnus pipes some 250 km to the north (Figure 1). Very little data is available on these rocks in the literature, which is practically limited to a study of mantle xenoliths from the Drybones Bay pipe [3] and U-Pb geochronological determinations for several of these bodies [4]. This lack of information is regrettable because (1) the majority of tested kimberlites from this part of the craton were found to be diamondiferous; (2) geologically, these localities are separated from the other Slave fields by a major crustal-scale fault (see Regional Geology), and (2) similar-aged economic pipes are known in the North China and Siberian cratons, where they have been studied extensively [5,6]. The present project was initiated to examine the petrology, mineralogy, and geochemistry of the SW Slave kimberlites using extensive exploration data and drill-core material available at the Geological Materials Storage facility operated by the Northwest Territories Geological Survey. This contribution is concerned with the trace element and isotopic characteristics of zircon from the Drybones Bay pipe.

This mineral was chosen because of its recognized value as a geochronometer, geothermometer and process indicator in the study of kimberlites and other mantle-derived rocks.

2. Geological Setting

2.1. Regional Geology

About one-third of the presently exposed Archean bedrock in the Slave craton is represented by metasedimentary and metavolcanic supracrustal rocks of the Yellowknife Supergroup (2.61–2.71 Ga), whereas some 65% is underlain by 2.58–2.64 Ga granitoid intrusions [7]. The Slave craton has been subdivided into eastern and western domains, based primarily on the presence of 2.85–4.05 Ga Mesoarchean rocks and Pb-Nd isotopic variations [8,9]. The Mesoarchean rocks comprise tonalitic to dioritic gneisses that so far have been reported only in the western domain [10]. Lower crustal xenoliths from kimberlites in the Lac de Gras area (Figure 1) indicate the presence of Mesoarchean rocks also east of the domain boundary [11]. The gneisses are overlain by a post-2.93 Ga autochthonous cover sequence, which forms the base of the Yellowknife Supergroup [10]. Supracrustal packages that can be correlated across the entire craton include 2.66–2.69 Ga calc-alkaline subvolcanic-to-extrusive units and younger (2.63–2.66 Ga) turbidites [12]. Syn- to late-kinematic granitoid plutons are voluminous and widespread [7], but intrusions older than 2.61 Ga are limited to the southwestern part of the craton, including the tonalite-granodioritic Defeat suite (ca. 2.62–2.63 Ga) at Drybones Bay. Widespread felsic magmatism spanning the entire craton occurred from ca. 2.61 to 2.58 Ga, and produced both I- and S-type granitoids [13]. Kimberlites are the most widespread form of post-Archean small-volume mantle-derived magmatism in the Slave craton. It spans a period of ~560 Ma from the emplacement of the 613-Ma Anuri pipe to the eruption of Eocene kimberlites in the Lac de Gras area [14,15]. There is a distinct correlation between the spatial distribution of kimberlites and the timing of magmatism, which allows the craton to be subdivided into four domains (Figure 1): (1) southwestern, hosting Siluro-Ordovician (435–459 Ma) pipes; (2) southeastern, characterized by Cambrian (523–542 Ma) kimberlites; (3) central, represented by Cretaceous to Eocene (48–74 Ma) localities; and (4) northern or "mixed", hosting the Jurassic (173 Ma) Jericho pipe, Permian-Triassic (245–286 Ma) Victoria Island and Ediacaran (613 Ma) Coronation Gulf fields [4,15]. The reason for this distribution of kimberlite ages is presently unknown. The sublongitudinal boundary of the southwestern domain roughly coincides with the exposed margin of the Mesoarchean rocks, and the kimberlites of this domain (including Drybones Bay) define a linear N-S trend, which parallels the crustal-scale Beniah Lake fault system [4].

2.2. Local Geology and Exploration History

The Drybones Bay kimberlite "pipe" is situated in a small bay on the northern shore of Great Slave Lake 45 km SE of Yellowknife. The body is submerged under 38 m of water and blanketed by 67 m of overburden, which consists of lacustrine clay, sand, and a basal layer of boulder conglomerate [16]. It intruded the 2.62–2.63 Ga Defeat pluton comprising predominantly biotite tonalite and granodiorite with minor metasedimentary xenoliths derived from the Yellowknife Supergroup [17]. The kimberlite body is interpreted to be a vent-like structure from drilling and geophysical surveys [18,19], but it is unknown how its morphology or size change with depth. The deepest drill hole (302 m) was stopped in volcaniclastic kimberlite. The structure is lobate in shape and measures ~900 × 400 m, covering an estimated area of 22 ha at the present erosion level [16]. The sidewall contacts dip at a lower angle in the western lobe relative to the eastern lobe. The large size and shallow dipping contacts are characteristic of Canadian Class-2 kimberlites, rather than Class-3 pipes characteristic of the central Slave domain [19,20]. The Drybones Bay structure comprises a core intrusion (termination of a feeder dike?), several crater-facies units and an epiclastic unit [16,17]. Unambiguous tuffisitic facies are notably absent.

During the staking rush of the 1990s, diamond exploration on the northern shore of Great Slave Lake led to the discovery of a geophysical anomaly submerged beneath Drybones Bay (Figure 1).

The anomaly was staked and drilled in the winter of 1994; 24 m of kimberlite was intersected under a blanket of lacustrine clay. Low-level airborne and ground-based magnetic surveys were conducted over the claim block over the following year to delineate the kimberlite body with more precision. This was followed by two extensive drill programs (1995 and 1996) that included 20 holes ranging from 131 to 302 m in length and produced over 5.5 km of drill-core. Most of the recovered kimberlite core was split and processed by caustic fusion. Three samples weighing 0.64, 1.87, and 7.58 tonnes yielded 16, 26, and 48 macrodiamonds, respectively, measuring >0.5 mm in at least one dimension [21]. Diamonds have been recovered from each of the lithostratigraphic units, but the highest exploration grades (24–39 carats per hundred tonnes) were measured for the core [16]. In the past 24 years, the Drybones Bay project has changed hands several times and been the subject of litigation between developers and Aboriginal groups [22].

3. Materials and Methods

Cathodoluminescence (CL) images were obtained using a Reliotron VII instrument (Relion Ind., Bedford, MA, USA) operated at 8.5 eV and 400–450 mA, and an electronically cooled Nikon DS-Ri1 camera (Nikon Canada Inc., Mississauga, ON, Canada). The concentrations of major elements were determined by wavelength-dispersive spectrometry (WDS) using a Cameca SX100 (Cameca SAS, Gennevilliers, France) automated electron microprobe operated at 15 kV and 20 nA. The CL and BSE images were used for the selection of areas suitable for further trace element and isotopic analyses.

The abundances of selected trace elements and isotopes were measured by laser-ablation inductively coupled-plasma mass-spectrometry (LA-ICP-MS) using a 213-nm Nd-YAG laser (Elemental Scientific Lasers, Bozeman, MT, USA) connected to an Element 2 sector-field mass-spectrometer (Thermo Fisher Scientific Inc., Bremen, Germany). The zircon grains were analyzed in situ using a spot ablation mode and the following laser parameters: 30 μm beam size, ~0.03 mJ incident pulse energy, 3.1–4.0 J/cm^2 energy density on a sample. Areas suitable for analysis were selected on the basis of reflected-light, BSE, and CL images. The ablation was performed in Ar and He atmospheres. The rate of oxide production was monitored during instrument tuning by measuring the ThO/Th ratio and kept below 0.2%. For LA-ICP-MS measurements, synthetic glass standard NIST SRM 610 [23] was employed for calibration and quality control. After considering potential spectral overlaps and molecular interferences, the following isotopes were chosen for analysis: ^{25}Mg, ^{29}Si, ^{45}Sc, ^{49}Ti, ^{51}V, ^{55}Mn, ^{88}Sr, ^{89}Y, ^{93}Nb, ^{139}La, ^{140}Ce, ^{141}Pr, ^{146}Nd, ^{147}Sm, ^{151}Eu, ^{157}Gd, ^{159}Tb, ^{163}Dy, ^{165}Ho, ^{167}Er, ^{169}Tm, ^{172}Yb, ^{175}Lu, ^{178}Hf, ^{181}Ta, ^{208}Pb, ^{232}Th, and ^{238}U. Silicon, measured by WDS, was employed as an internal standard. All analyses were performed in a low-resolution mode (~300) using Pt skimmer and sample cones.

The U-Pb geochronology of major zircon varieties was investigated using 100 μm spot analyses obtained at a repetition rate of 10 Hz with an incident laser beam pulse energy of 0.605–0.620 mJ and energy density on sample in the range 7.6–8.0 J/cm^2. The detector was operated in counting mode (^{235}U, ^{232}Th, ^{206}Pb, ^{207}Pb, ^{202}Pb, ^{202}Hg) and analogue mode (^{238}U). Natural zircon standard GJ-1 (609 Ma; [24] was employed for calibration, and was run at the beginning, in the middle, and at the end of each analytical session. Natural zircon FC-1 (1099 ± 0.6 Ma; [25]) was used as a secondary standard, yielding accuracy and precision levels near 2%. The data reduction was done using the VisualAge DRS procedure [26] in the Iolite software [27]. A Concordia diagram showing 2σ error ellipses was produced using Isoplot/Ex 3.75 [28].

4. Results

4.1. CL Imaging

The examined zircon grains are macroscopically brown in color, homogeneous in transmitted light and BSE images, and vary from small angular fragments to large subhedral crystals reaching several mm in size. Cathodoluminescence revealed significant variations in the distribution of CL-active

centers in the Drybones Bay zircons and their internal complexity (Figures 1 and 2). Based on their luminescence characteristics, several types of zircon were distinguished:

- Type 1: oscillatory-zoned yellow to brown in CL images (Figure 2a);
- Type 2: broad brown zones confined to blue-luminescing areas (Figure 2b);
- Type 3: light blue, homogeneous or subtly zoned (Figure 2c);
- Type 4: patchy yellow to greenish-yellowish (Figure 2d);
- Type 5: yellowish-grey (Figure 2e);
- Type 6: zoned dark-blue with brownish overtones (Figure 2f).

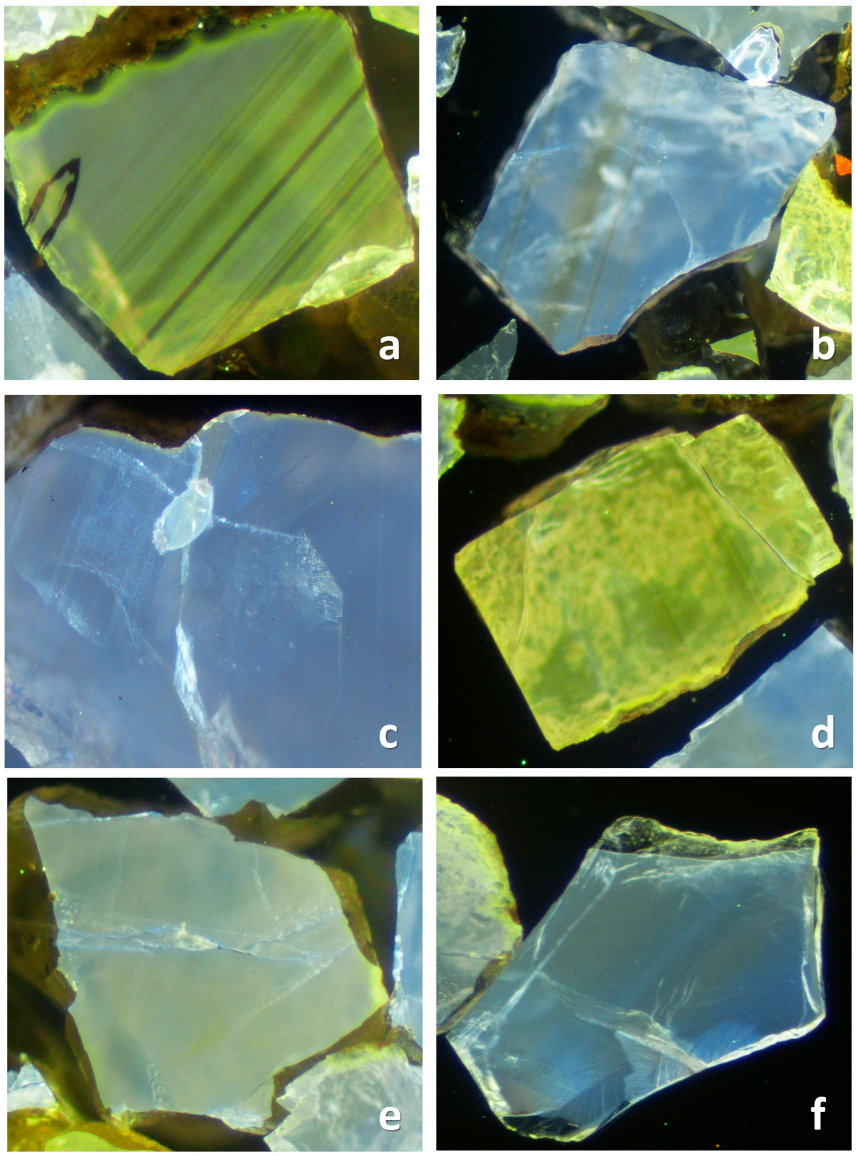

Figure 2. Cathodoluminescence images of zircon from the Drybones Bay kimberlite: (**a**) Oscillatory-zoned crystal of Type 1 (0.6 mm across); (**b**) zoned crystal comprising Type 2 (wide brown band 0.06 mm in thickness) and Type 3 (blue areas); (**c**) blue-luminescing zircon of Type 3 (width of the field of view 1.25 mm); (**d**) patchy (greenish) yellow grain of Type 4 (0.75 mm in length); (**e**) yellowish-grey Type 5 (0.65 mm across); (**f**) dark brownish-blue luminescence in Type 6 (0.8 mm in ength).

In many cases, more than one type of luminescence is present within a single zoned grain, commonly as concentric growth zones (e.g., Figure 2a,b,f and Figure 3a). In addition, several large

zircon grains exhibit a sector pattern consisting of bright yellow and light blue sectors (types 3 and 4, respectively) separated by a well-defined boundary (Figure 3b). The CL features revealed in the present work, including oscillatory zoning (Type 1), broad bands (Type 2), and irregularly shaped areas (Type 5), have been previously observed in zircon from other kimberlite localities, often in the same grain [29–31].

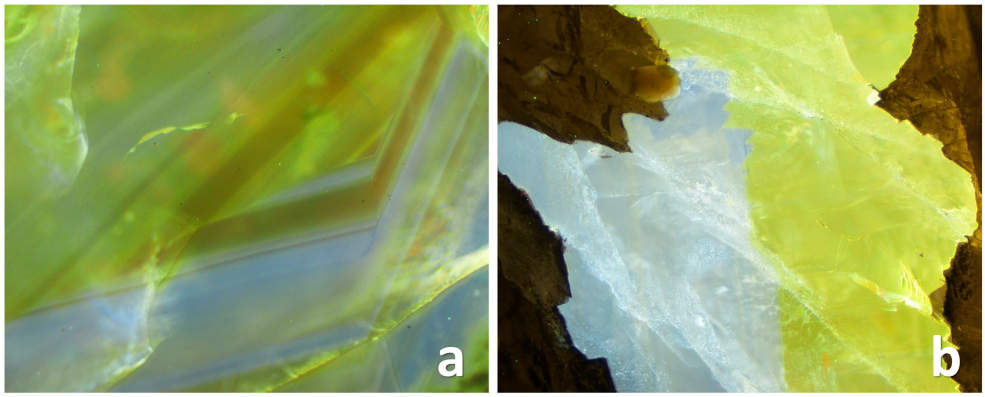

Figure 3. Cathodoluminescence images of zoned zircon from the Drybones Bay kimberlite (width of the field of view is 1.25 mm for both images): (**a**) oscillatory-zoned core (Type 1) rimmed by Type 3 zircon; (**b**) sector-zoned grain comprising Type 3 and Type 4 domains.

4.2. Trace Element Composition and Variations

In this work, we studied zircon grains with all types of CL response. In total, 90 trace-element analyses were done in samples imaged using CL. Our data show that the Drybones Bay zircon macrocrysts exhibit appreciable variations in trace element abundances and ratios, particularly with regard to rare-earth elements (REE = La-Lu). All samples are relatively enriched in Ta (1.8–12.3 ppm), but contain moderate levels of Hf (8200–10,900 ppm) at low levels of REE (<1.5 ppm Lu, <60 ppm Y). None of the seven types exhibit Eu anomalies. The average δEu ratio, which reflects deviation of the Eu concentration from a value interpolated from the chondrite-normalized Sm and Gd abundances, and is measured as $Eu_{cn}/[0.5 \times (Sm_{cn} + Gd_{cn})]$, is 1.0 ± 0.2. These compositional characteristics are consistent with kimberlitic zircon [32] and rule out crustal rocks or the Defeat granitoids as a potential source of these macrocrysts (cf. [33]). Another notable characteristic of the studied material is its enrichment in Sc (570–930 ppm), which is far in excess of what has been reported for felsic rocks [34].

The most significant compositional differences are observed between grains showing blue and yellow luminescence (Table 1), in accord with the observations made previously by Belousova et al. [30]. Areas luminescing blue show the lowest levels of REE and Y (5–10 ppm and 6–11 ppm, respectively, in Type 3; 12–18 and 14–22 ppm, respectively, in Type 6; Figure 4a). In contrast, those showing yellow or yellowish-brown response contain the highest levels of these elements among the examined samples (23–53 ppm REE and 26–59 ppm Y in Type 1; 19–33 and 21–36 ppm, respectively, in Type 4). These differences are particularly striking in sector-zoned grains (Figure 3b), where REE+Y levels increase two- to fourfold across the sector boundary (Figure 4a). These variations are not accompanied by any consistent changes in Sc content. Grains showing yellow luminescence are also enriched in Th and U (3–9 and 8–20 ppm, respectively, in Type 1) relative to blue areas (≤2 ppm Th and ≤5 ppm U in Types 3 and 6; Figure 4b). The Th/U ratio (Figure 4c) tends to be somewhat higher in Type-1, -4, and -5 zircon (0.31–0.47) relative to the blue-luminescing material (0.22–0.40), but overall shows little variation (average Th/U = 0.34 ± 0.07). The abundances of Nb and Ta are comparable in sector-zoned crystals (Types 3 and 4 in Figure 4d) and reach their maximum values in brown growth zones, such as those shown in Figure 2a,b (up to 11 ppm Nb and 8 ppm Ta in Type 1, and up to 12 ppm of both in Type 2). The Nb/Ta ratio is strongly subchondritic and only slightly higher in the oscillatory-zoned core (1.1 ± 0.1) relative to the rest of the data (0.98 ± 0.08; Figure 4e). The highest

Ti contents (21–34 ppm) are observed in the core (Figure 4c). Titanium levels are lower (10–25 ppm) and comparable in sector-zoned (Type-3 and -4) and blue-luminescing zircon. The latter is richer in Hf (9500–10,900 ppm) than the oscillatory core and yellow sectors (8200–9400 ppm), which is reflected in Zr/Hf variations depicted in Figure 4e. As can be expected, the Pb content reaches maximum values in U- and Th-rich zones (0.09–0.26 ppm), and ranges from levels below the LA-ICP-MS detection limit to 0.11 ppm in U-Th-poor blue-luminescing zircon (Figure 4f). Type 5 is compositionally transitional between Types 3 and 4.

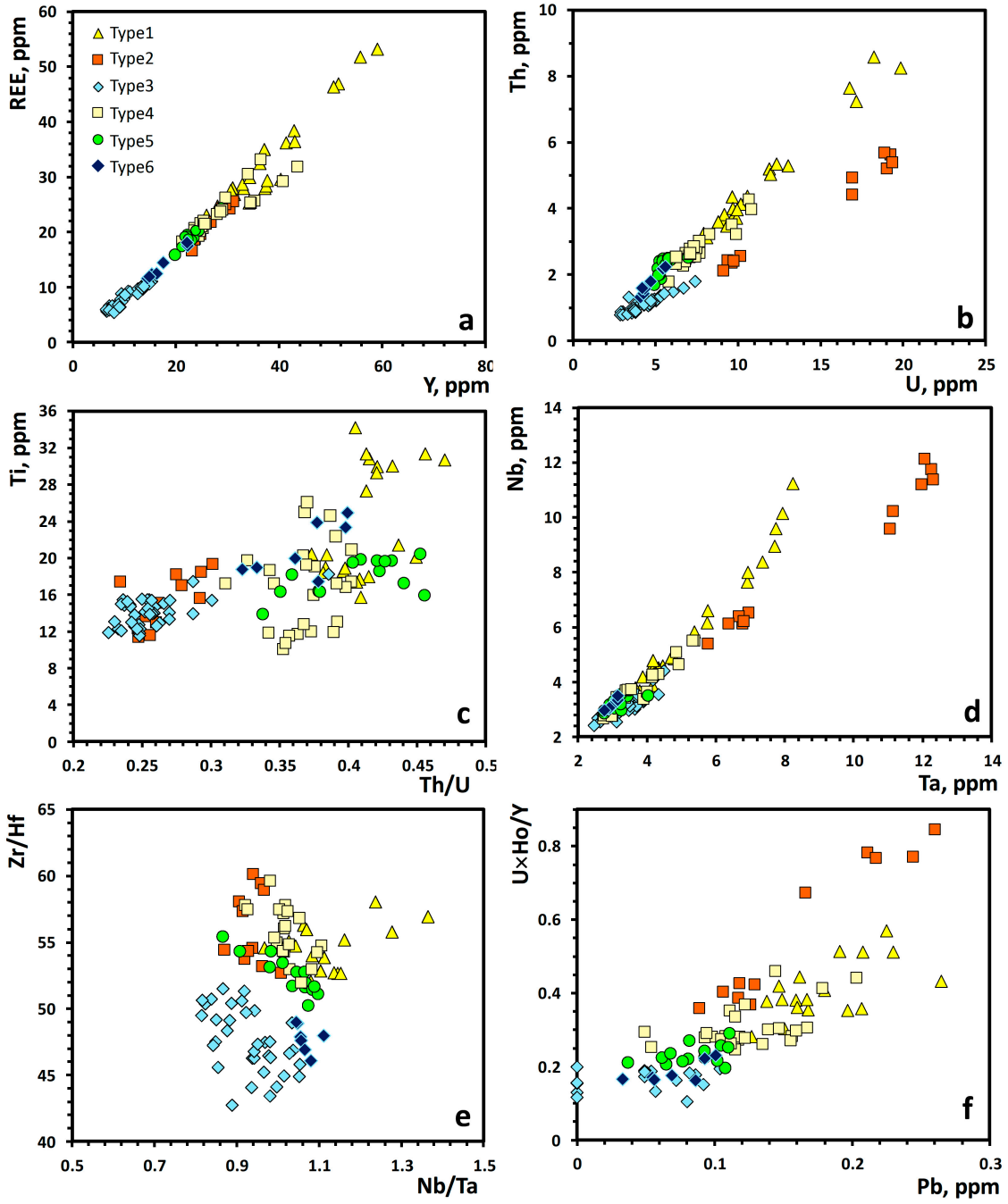

Figure 4. Variations in trace element composition among different types of zircon (distinguished on the basis of their cathodoluminescence (CL) characteristics).

Table 1. Trace element composition of zircon from Drybones Bay kimberlite.

Element	Type 1			Type 2			Type 3			Type 4			Type 5			Type 6		
	Min	Max	Av	Min	Max	Av	Min	Max	Av	Min	Max	Av	Min	Max	Av	Min	Max	Av
Ti	15.72	34.18	24.93	11.43	19.34	15.09	12.30	14.35	18.21	10.09	20.27	14.07	13.85	20.42	17.96	17.45	24.95	21.03
V	0.10	0.36	0.20	0.09	0.22	0.13	0.08	0.11	0.17	0.10	0.16	0.14	0.08	0.17	0.12	0.07	0.17	0.13
Mn	0.33	0.33	0.33	0.29	0.75	0.52	0.39	0.39	0.39	b.d.l.	b.d.l.	b.d.l.	0.27	0.27	0.27	b.d.l.	b.d.l.	b.d.l.
Sr	0.33	0.36	0.34	0.25	0.62	0.37	0.23	0.37	0.55	0.41	0.41	0.41	b.d.l.	b.d.l.	b.d.l.	b.d.l.	b.d.l.	b.d.l.
Y	25.99	59.04	39.12	23.54	31.15	26.89	6.51	8.73	11.01	21.20	36.43	26.34	19.79	28.87	23.16	14.47	22.32	17.57
Nb	3.67	11.24	6.69	6.14	12.14	8.89	2.40	2.98	3.54	2.68	5.51	3.35	2.86	3.53	3.20	2.95	3.50	3.19
La	b.d.l. [1]	0.09	0.04	b.d.l.	0.10	0.01	b.d.l.	b.d.l.	b.d.l.	b.d.l.	0.06	0.03	b.d.l.	0.02	b.d.l.	b.d.l.	b.d.l.	b.d.l.
Ce	1.20	3.13	1.84	1.10	1.77	1.44	0.67	0.75	0.94	0.99	1.49	1.17	0.80	1.07	1.00	0.85	1.10	0.94
Pr	0.03	0.16	0.09	b.d.l.	0.04	0.02	b.d.l.	0.01	0.03	b.d.l.	0.10	0.04	b.d.l.	0.06	0.02	b.d.l.	0.03	0.01
Nd	0.82	2.53	1.39	0.19	0.74	0.37	b.d.l.	0.19	0.37	0.42	1.29	0.69	0.26	0.81	0.53	0.18	0.44	0.33
Sm	0.94	2.89	1.48	0.28	0.69	0.51	0.13	0.26	0.43	0.53	1.28	0.89	0.47	0.89	0.69	0.24	0.55	0.42
Eu	0.52	1.28	0.81	0.25	0.45	0.34	0.08	0.11	0.23	0.33	0.71	0.47	0.23	0.49	0.38	0.17	0.35	0.26
Gd	2.10	6.09	3.70	0.92	2.39	1.69	0.32	0.53	1.05	1.50	3.72	2.22	1.37	2.48	1.84	0.82	1.84	1.27
Tb	0.49	1.20	0.82	0.35	0.58	0.45	0.08	0.14	0.19	0.41	0.77	0.54	0.34	0.55	0.44	0.24	0.41	0.31
Dy	4.34	10.37	6.86	3.64	4.93	4.21	0.92	1.30	1.76	3.40	6.59	4.54	3.28	4.68	3.93	2.27	3.76	2.84
Ho	1.06	2.37	1.66	0.93	1.32	1.13	0.25	0.34	0.43	0.94	1.58	1.11	0.84	1.20	0.97	0.58	0.94	0.70
Er	3.05	7.30	4.96	2.90	4.17	3.52	0.78	1.13	1.48	2.43	4.88	3.31	2.44	3.62	2.93	1.78	2.91	2.22
Tm	0.62	1.38	0.98	0.59	0.87	0.74	0.16	0.23	0.34	0.58	0.98	0.67	0.47	0.73	0.57	0.35	0.49	0.42
Yb	6.61	14.36	9.49	5.96	8.01	6.87	1.55	2.22	2.93	5.52	9.74	6.43	3.95	7.33	5.46	3.21	5.05	3.98
Lu	0.51	1.25	0.84	0.57	0.72	0.65	0.12	0.22	0.30	0.46	0.73	0.57	0.42	0.69	0.51	0.32	0.48	0.39
Hf	8439	9411	8982	8154	9287	8753	9502	10,033	10,873	8211	9243	8689	8839	9738	9321	9985	10,595	10,237
Ta	3.79	8.23	5.86	6.36	12.30	9.48	2.46	3.33	4.34	2.73	5.38	3.32	2.76	4.04	3.13	2.77	3.15	2.99
Pb	0.13	0.38	0.23	0.11	0.31	0.18	0.03	0.05	0.08	0.05	0.18	0.11	0.04	0.11	0.09	0.03	0.10	0.07
Th	2.62	8.58	5.05	2.37	5.69	3.95	0.77	0.98	1.31	1.80	4.28	2.67	1.67	2.51	2.25	1.32	2.23	1.73
U	6.86	19.86	11.93	9.35	19.34	14.42	2.86	3.64	4.61	5.78	10.65	7.20	4.95	6.99	5.55	4.09	5.58	4.66
ΣREE	23.01	53.20	34.92	18.60	25.64	21.95	5.62	7.37	9.32	18.36	33.17	22.64	15.90	24.37	19.27	11.60	18.13	14.08
Nb/Ta	0.97	1.37	1.12	0.87	1.01	0.94	0.82	0.90	1.05	0.92	1.11	1.01	0.87	1.10	1.03	1.04	1.11	1.07
Zr/Hf	52	58	55	53	60	56	45	49	51	53	60	56	50	55	53	46	49	48
Y/Ho	22	26	24	22	25	24	22	26	28	22	26	24	21	26	24	24	27	25
Th/U	0.38	0.47	0.42	0.25	0.30	0.27	0.23	0.27	0.39	0.31	0.40	0.37	0.34	0.46	0.40	0.32	0.40	0.37
$(Nd/Yb)_{cn}$	0.04	0.07	0.05	0.01	0.04	0.02	0.01	0.04	0.08	0.03	0.05	0.04	0.02	0.05	0.04	0.02	0.04	0.03
δCe	3.9	9.0	5.3	6.2	15.7	11.4	5.3	7.0	7.8	3.5	9.1	6.3	4.1	10.3	7.5	6.8	13.2	10.8

[1] b.d.l.: below detection limit.

The REE budget of all six zircon varieties is very similar. Chondrite-normalized patterns show a steep slope rising towards heavy lanthanides (Nd_{cn}/Yb_{cn} = 0.036 ± 0.015), with a conspicuous positive Ce anomaly (Figure 5). The average δCe value, measured as $Ce_{cn}/[0.5 \times (La_{cn} + Pr_{cn})]$, is 8.2 ± 3.9, and none of the individual varieties give δCe below 3.5. Neither Eu nor Y anomalies are observed, and the average Y/Ho ratio is essentially chondritic (25 ± 2). The REE characteristics of zircon (i.e., the shape of chondrite-normalized profiles, Ce, Eu, and Y anomalies) are sensitive to its interaction with fluids and melts [33,35,36]. Because the Y/Ho ratio shows the least variation across the dataset, we used it as a "common denominator" to gauge the extent of Pb loss (or gain). In Figure 4f, we compare variations in Pb to the measured U values normalized to the Y/Ho ratio in the same analysis. There is a clear positive correlation (R^2 = 0.79) between the two parameters, and no obvious outliers that would indicate variations in Pb content beyond those caused by heterogeneities in U distribution.

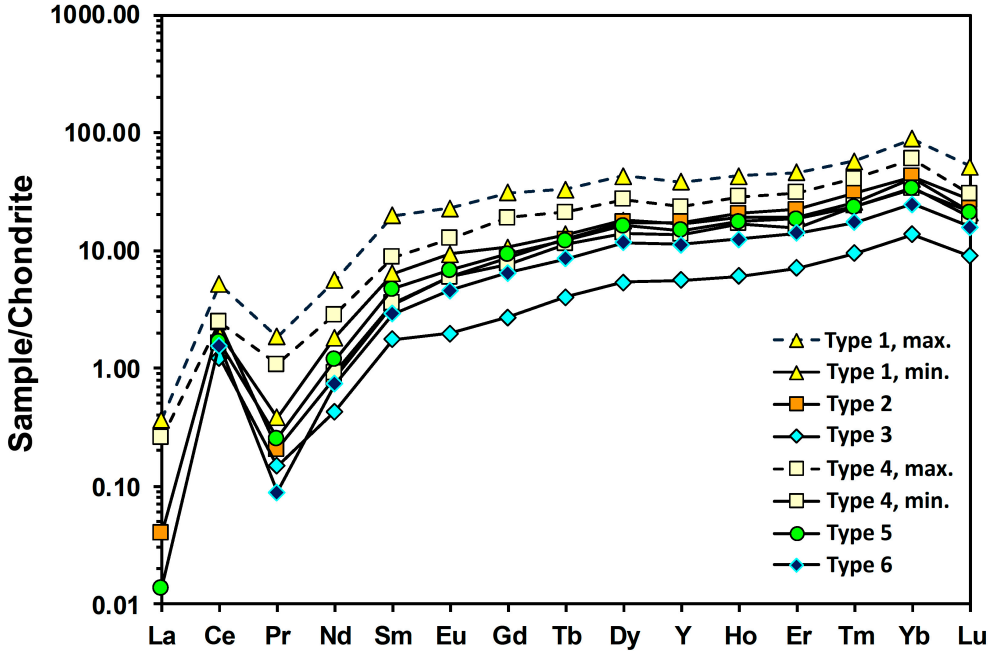

Figure 5. Chondrite-normalized patterns of the different types of zircon from the Drybones Bay kimberlite (lower limits of detection are plotted for La and Pr where these elements were not detectable by LA-ICP-MS).

4.3. Thermometry

The concentration of Ti in the analyzed macrocrysts ranges between 10 and 34 ppm (Figure 4c). The oscillatory-zoned core, which fluoresces from yellow to yellowish-brown, shows the highest levels of this element, suggesting its crystallization at relatively higher temperature. Crystals showing sector zoning (Types 3 and 4) and brown zones in these crystals (Types 2 and 6) have overlapping Ti levels. The Ti-in-zircon thermometer of Watson et al. [37] gives apparent crystallization temperatures spanning from 742 °C (yellow sector) to 862 °C (core; Table 2). The average estimated temperatures are 820 ± 26 °C for the core and 781 ± 19 °C for the rest of the data, i.e., essentially within the estimated standard deviation of each other.

Table 2. Variations in Ti content and estimated crystallization temperatures of zircon from the Drybones Bay kimberlite.

Parameter	Type 1	Type 2	Type 3	Type 4	Type 5	Type 6
Ti (ppm) ± SD	24.9 ± 6.2	15.1 ± 2.9	14.6 ± 1.9	14.1 ± 3.1	18.0 ± 2.0	21.0 ± 3.0
Average T (°C ± SD)	825 ± 27	777 ± 18	775 ± 12	770 ± 20	795 ± 11	810 ± 14
# analyses	18	11	18	15	14	7

4.4. U-Pb Geochronometry of Zircon from the Drybones Bay Kimberlite

The U-Pb isotopic study of zircon from the Drybones Bay kimberlite was performed on three large (several mm across) anhedral grains showing essentially the entire range of variations in CL. In total, 80 points were analyzed. Data reduction showed that, whereas the majority of the data points formed a fairly tight cluster on the Concordia diagram, some of the analyses were not concordant and corresponded either to notably younger or older ages than the rest of the data. Closer inspection of these points showed that most of these analyses were performed close to the visible cracks or grain boundaries. Eventually, 63 data points were used for the calculation of zircon crystallization age, yielding a well-constrained value of 445.6 ± 0.8 Ma (Figure 6). The isotopic ratios and calculated ages for all data points are presented in Table 3.

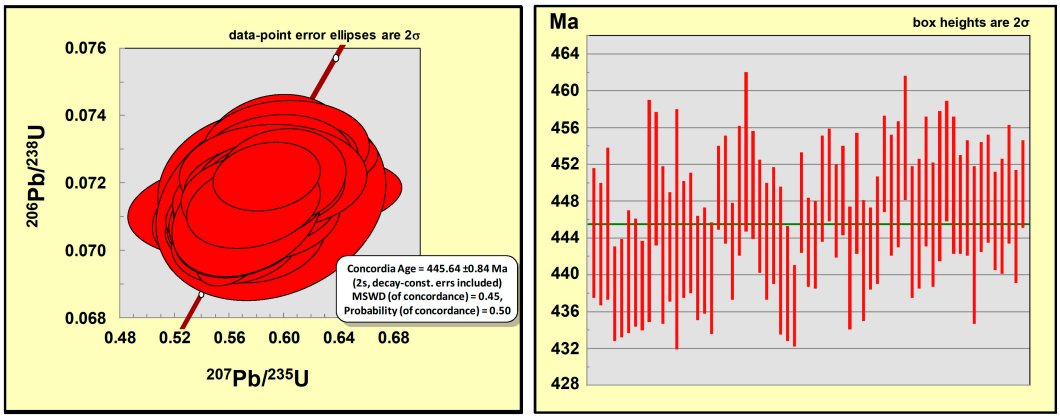

(**a**) (**b**)

Figure 6. U-Pb data for zircon macrocrysts (all CL types) from the Drybones Bay kimberlite: (**a**) Concordia diagram; (**b**) weighted mean of $^{207}Pb/^{235}U$ ages.

Table 3. U-Pb isotopic data for zircon from the Drybones Bay kimberlite.

Analysis	Measured Ratios						Age, Ma	
	$^{207}Pb/^{235}U$	±2σ	$^{206}Pb/^{238}U$	±2σ	$^{207}Pb/^{206}Pb$	±2σ	$^{206}Pb/^{238}U$	±2σ
1	0.5500	0.0460	0.0714	0.0012	0.0558	0.0047	445	7
2	0.5560	0.0220	0.0712	0.0011	0.0564	0.0021	443	7
3	0.5500	0.0370	0.0716	0.0014	0.0557	0.0035	446	8
4	0.5380	0.0220	0.0703	0.0008	0.0554	0.0022	438	5
5	0.5410	0.0230	0.0704	0.0009	0.0555	0.0023	439	5
6	0.5400	0.0200	0.0707	0.0011	0.0553	0.0021	440	7
7	0.5410	0.0230	0.0707	0.0010	0.0556	0.0024	440	6
8	0.5390	0.0250	0.0705	0.0008	0.0554	0.0025	439	5
9	0.5550	0.0390	0.0718	0.0019	0.0565	0.0043	447	12
10	0.5600	0.0310	0.0724	0.0012	0.0560	0.0032	451	7
11	0.5530	0.0330	0.0712	0.0014	0.0565	0.0034	443	9
12	0.5470	0.0300	0.0712	0.0010	0.0557	0.0031	443	6
13	0.5590	0.0430	0.0715	0.0022	0.0566	0.0042	445	13
14	0.5460	0.0270	0.0713	0.0011	0.0555	0.0027	444	6
15	0.5510	0.0270	0.0714	0.0011	0.0559	0.0028	445	7
16	0.5450	0.0280	0.0708	0.0009	0.0557	0.0029	441	6
17	0.5410	0.0240	0.0709	0.0009	0.0553	0.0024	442	6
18	0.5410	0.0180	0.0706	0.0010	0.0553	0.0019	440	6
19	0.5550	0.0190	0.0722	0.0008	0.0556	0.0019	450	5
20	0.5570	0.0230	0.0722	0.0010	0.0558	0.0023	449	6
21	0.5450	0.0160	0.0711	0.0009	0.0555	0.0017	443	5
22	0.5640	0.0270	0.0722	0.0012	0.0563	0.0026	449	7
23	0.5610	0.0280	0.0729	0.0014	0.0560	0.0028	453	9
24	0.5570	0.0220	0.0723	0.0010	0.0559	0.0023	450	6
25	0.5530	0.0250	0.0717	0.0010	0.0557	0.0025	446	6

Table 3. *Cont.*

Analysis	Measured Ratios						Age, Ma	
	$^{207}Pb/^{235}U$	±2σ	$^{206}Pb/^{238}U$	±2σ	$^{207}Pb/^{206}Pb$	±2σ	$^{206}Pb/^{238}U$	±2σ
26	0.5490	0.0310	0.0713	0.0010	0.0558	0.0030	444	6
27	0.5500	0.0210	0.0715	0.0010	0.0557	0.0022	445	6
28	0.5490	0.0290	0.0709	0.0013	0.0561	0.0031	442	8
29	0.5430	0.0240	0.0705	0.0010	0.0559	0.0025	439	6
30	0.5410	0.0130	0.0701	0.0007	0.0557	0.0012	437	4
31	0.5550	0.0120	0.0720	0.0009	0.0558	0.0013	448	5
32	0.5480	0.0200	0.0713	0.0008	0.0556	0.0020	444	5
33	0.5480	0.0150	0.0712	0.0008	0.0557	0.0016	443	5
34	0.5560	0.0180	0.0722	0.0010	0.0558	0.0018	449	6
35	0.5610	0.0150	0.0725	0.0008	0.0561	0.0015	451	5
36	0.5550	0.0130	0.0718	0.0008	0.0558	0.0012	447	5
37	0.5570	0.0210	0.0722	0.0008	0.0558	0.0021	449	5
38	0.5440	0.0240	0.0708	0.0011	0.0557	0.0024	441	7
39	0.5560	0.0260	0.0721	0.0011	0.0557	0.0027	449	7
40	0.5430	0.0250	0.0709	0.0011	0.0555	0.0027	442	7
41	0.5500	0.0200	0.0711	0.0007	0.0558	0.0021	443	4
42	0.5510	0.0300	0.0715	0.0010	0.0559	0.0031	445	6
43	0.5640	0.0360	0.0727	0.0009	0.0562	0.0035	452	5
44	0.5590	0.0330	0.0721	0.0011	0.0560	0.0031	449	7
45	0.5680	0.0270	0.0723	0.0011	0.0568	0.0027	450	7
46	0.5660	0.0310	0.0731	0.0011	0.0562	0.0032	455	7
47	0.5540	0.0300	0.0714	0.0012	0.0563	0.0031	445	7
48	0.5510	0.0280	0.0716	0.0012	0.0559	0.0030	446	7
49	0.5610	0.0310	0.0723	0.0012	0.0558	0.0028	450	7
50	0.5520	0.0310	0.0716	0.0011	0.0559	0.0032	446	7
51	0.5610	0.0260	0.0723	0.0013	0.0565	0.0028	450	8
52	0.5610	0.0290	0.0727	0.0011	0.0559	0.0028	452	7
53	0.5600	0.0350	0.0723	0.0012	0.0563	0.0035	450	7
54	0.5530	0.0230	0.0719	0.0009	0.0555	0.0021	448	5
55	0.5560	0.0300	0.0720	0.0010	0.0559	0.0030	448	6
56	0.5480	0.0280	0.0712	0.0014	0.0554	0.0028	443	9
57	0.5550	0.0250	0.0721	0.0010	0.0558	0.0025	449	6
58	0.5550	0.0250	0.0722	0.0010	0.0556	0.0024	449	6
59	0.5530	0.0230	0.0716	0.0009	0.0559	0.0024	446	5
60	0.5510	0.0270	0.0717	0.0010	0.0557	0.0028	446	6
61	0.5640	0.0240	0.0723	0.0011	0.0564	0.0024	450	6
62	0.5510	0.0250	0.0715	0.0010	0.0557	0.0025	445	6
63	0.5570	0.0200	0.0723	0.0008	0.0557	0.0020	450	5

5. Discussion

Large (mm- to cm-sized) zircon fragments, referred to as macro- or megacrysts, occur in a variety of volcanic rocks, including kimberlites, lamprophyres, and alkali basaltoids [31,38,39]. Apart from their large size, seemingly inconsistent with crystallization from a rapidly ascending melt, these macrocrysts share a number of characteristics [31,38–44]:

1. Complex internal structures involving sector and/or oscillatory zoning (as revealed by high-resolution CL imaging) and arising from multistage growth (±resorption);
2. Low Ti contents (<60 and typically, ≤30 ppm) indicative of relatively low crystallization temperatures (typically, ≤850 °C);
3. Chondrite-normalized patterns steeply sloping up towards the heavy lanthanides and characterized by a positive Ce anomaly (δCe in excess of 100 in some cases);
4. Variable, chondritic to strongly superchondritic (~80) Zr/Hf ratios;
5. Highly variable (over one order of magnitude) Th and U abundances and variable, but consistently subchondritic (0.2–1.7) Th/U ratios;
6. U-Pb ages similar to those of their host igneous rock.

Presently, there is no consensus on the origin of these enigmatic crystals. Three principally different interpretations have been proposed in the previous literature, i.e., that:

I. They represent older mantle-derived xenocrysts entrained in ascending silica-undersaturated melts [4];
II. They crystallized in mantle rocks affected by metasomatism, possibly related to kimberlitic or alkali-basaltic magmatism, in their source [31,45];
III. They are early cognate phenocrysts that recorded evolution of their parental magma [38,42].

Macrocrysts from the Drybones Bay pipe were previously investigated by Heaman et al. [4], who interpreted them to derive from a Mesoproterozoic, deep (~1.0 Ga, >150 km) mantle source, and to have remained open to Pb diffusion prior to their entrainment in kimberlite. The temperatures of zircon crystallization obtained in the present work cluster between 780 and 820 °C (Table 2). These values fall well within the temperature range (608–927 °C) determined for kimberlitic zircon from the Siberian, Kaapvaal, Amazonas, and São Francisco cratons by Page et al. [31]. When projected to the average Slave geotherm (Figure 7), our data plot above the field of mantle garnets from the Drybones Bay pipe analyzed by Carbno and Canil [3]. If the studied macrocrysts were indeed derived from a (metasomatized) mantle source, it had to be much shallower than 160 km (estimated from garnet-clinopyroxene equilibria by Carbno and Canil [3].

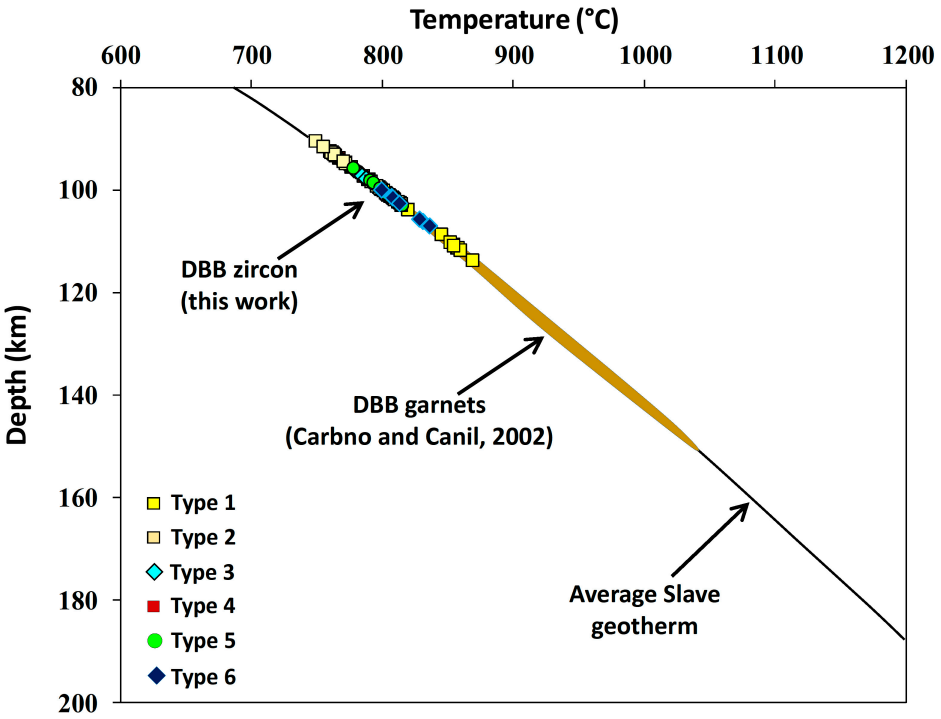

Figure 7. Estimated range of crystallization temperatures and depths for zircons (this work) and garnets [3] from Drybones Bay (DBB) projected on the average Slave Province geotherm.

Notably, the Zr/Hf ratio of our samples is consistently superchondritic (≥43 and, on average, 52 ± 4), i.e., departs significantly from the mantle values (~36–37: [46,47]). Published data on peridotite-hosted zircon are scarce, but suggest near-chondritic Zr/Hf values for this mineral [45,48,49]. Although it is possible that the trace element budget of the hypothetical mantle source was modified by its interaction with a metasomatizing agent, how likely is the ascending kimberlite to have caused the documented Zr-Hf decoupling? Kimberlites have near-chondritic Zr/Hf ratios [50], which are also observed at Drybones Bay: the average Zr/Hf value, calculated for 21 whole-rock analyses of uncontaminated samples, is 37.5 ± 1.6 at 390 ppm Zr and 10.4 ppm Hf (authors' unpublished data).

Assuming Rayleigh-style partitioning between a kimberlitic melt and zircon, Zr must partition into the latter ~1.4 times more effectively than Hf to cause the observed decoupling. Note that at very small (but realistic) degrees of fractionation (on the order of 0.01–0.001 wt %), the Zr-Hf budget of kimberlitic melt will not be perceptibly affected and will effectively maintain its near-chondritic Zr/Hf ratio. Unfortunately, Zr-Hf partitioning data are available only for silica-saturated systems, where both $^{Zrn/L}D_{Zr} > {}^{Zrn/L}D_{Hf}$ and $^{Zrn/L}D_{Hf} > {}^{Zrn/L}D_{Zr}$ have been documented (e.g., [51]). At very small degrees of fractionation, preferential uptake of Ce^{4+} by zircon [52] will have little effect on the REE budget of kimberlite because all light lanthanides are strongly incompatible with respect to this mineral. Indeed, the Drybones Bay whole-rock data do not show a Ce anomaly ($\delta Ce = 0.96 \pm 0.02$: authors' unpublished data).

Simonetti and Neal [38] described a trend of increasing Zr/Hf and REE content (39–50 and 20–100 ppm, respectively) in progressively younger zircon megacrysts from Malaita alnöites, Solomon Islands. These authors interpreted the compositional changes in zircon to reflect evolution of its parental alnöitic magma in response to mantle metasomatism. Although our dataset does show a weak correlation between the Zr/Hf and REE values ($R^2 = 0.35$), it is entirely due to overall higher REE and lower Hf abundances in yellow-luminescing areas in comparison with blue-luminescing ones (see above). These variations occur within individual sector-zoned crystals (Figure 3b), i.e., are controlled crystallographically [53]. Hence, we conclude that the data distributions in Figure 4a,e reflect growth phenomena, such as the different rates of REE and Hf uptake by symmetrically non-equivalent faces, rather than magma-evolution processes. Sector zoning, documented in the present work and several earlier studies [31,39,42,43], is indicative of relatively fast crystallization, i.e., not consistent with long residence times in the mantle.

In the present work, we did not observe any evidence of zircon re-equilibration with invading melts or fluids, such as overgrowths or fracture fillings differing from the bulk of the macrocrysts in their trace element budget (e.g., [33]). In fact, the measured REE distributions are remarkably consistent in the Drybones Bay samples irrespective of their CL response (Figure 5). Appreciable intragranular variations are recorded with respect to Nb, Ta, Th, and U contents but, again, correlate with growth sectors or concentric brown bands in dominantly yellow or blue-fluorescing areas (Figure 4b,d). These local fluctuations likely resulted from preferential uptake of these elements by specific crystal faces or changes in their availability due to competitive partitioning between zircon and other minerals.

The U-Pb isotopic data reported in the present work are in good agreement with the previously published "bulk" measurements obtained by thermal ionization mass-spectrometry (441.4 ± 0.8 Ma; [4]). Our data are concordant and do not show any convincing evidence of Pb mobilization by melts or fluids. The recorded variations in Pb within and among the macrocrysts (Figure 4f) can be explained by variations in U content (anchored to Y/Ho values) and do not seem to indicate any Pb loss either. The six types of zircon identified from CL images are considered cogenetic, rather than having been generated by interaction between Precambrian zircon xenocrysts and kimberlitic magma.

On the basis of the mineralogical and geochemical evidence presented above, we conclude that the Drybones Bay zircon macrocrysts most likely crystallized in a shallow (<100 km) mantle source due to its reaction with a transient kimberlitic melt. The conduit–melt interaction was short-lived and produced complexly zoned zircon crystals whose compositional heterogeneity results from interplay between element partitioning and crystallographically controlled uptake of trace elements. We found no evidence for the presence of ancient ($t >> 440$ Ma) zircon in the mantle source(s) of the Drybones Bay kimberlite.

Author Contributions: Conceptualization, A.R.C. and B.E.; methodology, A.R.C., E.P.R., and P.Y.; investigation, A.R.C., E.P.R., and A.R.S.; data curation, A.R.C., E.R., A.R.S., and P.Y.; writing—original draft preparation, A.R.C., E.P.R., and A.R.S.; writing—review and editing, A.R.C. and B.E.; visualization, A.R.C. and E.P.R.; funding acquisition, A.R.C. and B.E.

Funding: This research was funded by the NWT Geological Survey (contract number 63040) and Natural Sciences and Engineering Research Counsel of Canada (NSERC grant number 249596-2013).

Acknowledgments: We would like to thank Guest Editor Sergey Krivovichev for his invitation to contribute to the present issue. We are grateful to two anonymous reviewers who provided constructive comments on its earlier version. The NWT Government and NSERC are acknowledged for their financial support.

Conflicts of Interest: The authors declare no conflict of interest.

References

1. Government of NWT. 2016. Available online: https://www.iti.gov.nt.ca/sites/iti/files/mineraldeposites2-nocrops.pdf (accessed on 24 October 2018).
2. Pell, J.A. Kimberlites in the Slave Craton, Northwest Territories, Canada. *Geosci. Can.* **1997**, *24*, 77–90.
3. Carbno, G.B.; Canil, D. Mantle structure beneath the southwest Slave craton, Canada: Constraints from garnet geochemistry in the Drybones Bay kimberlite. *J. Petrol.* **2002**, *43*, 129–142. [CrossRef]
4. Heaman, L.M.; Kjarsgaard, B.A.; Creaser, R.A. Timing of kimberlite magmatism in North America: Implications for global genesis and diamond exploration. *Lithos* **2003**, *71*, 153–184. [CrossRef]
5. Yang, Y.-H.; Wu, F.-Y.; Wilde, S.A.; Liu, X.-M.; Zhang, Y.-B.; Xie, L.-W.; Yang, J.-H. In situ perovskite Sr–Nd isotopic constraints on the petrogenesis of the Ordovician Mengyin kimberlites in the North China Craton. *Chem. Geol.* **2009**, *264*, 24–42. [CrossRef]
6. Smelov, A.P.; Zaitsev, A.I. The age and localization of kimberlite magmatism in the Yakutian Kimberlite Province: Constraints from isotope geochronology—An overview. In *Proceedings of 10th International Kimberlite Conference*; Pearson, D.G., Grütter, H.S., Harris, J.W., Kjarsgaard, B.A., O'Brien, H., Rao, N.V.C., Sparks, S., Eds.; Springer: New Delhi, India, 2013; pp. 225–234. [CrossRef]
7. Padgham, W.A.; Fyson, W.K. The Slave Province: A distinct craton. *Can. J. Earth Sci.* **1992**, *29*, 2072–2086. [CrossRef]
8. Davis, W.J.; Hegner, E. Neodymium isotopic evidence for the accretionary development of the Late Archean Slave Province. *Contrib. Miner. Petrol.* **1992**, *111*, 493–503. [CrossRef]
9. Thorpe, R.I.; Cumming, G.L.; Mortensen, J.K. A Significant Pb Isotope Boundary in the Slave Province and Its Probable Relation to Ancient Basement in the Western Slave Province. Project Summaries, Canada Northwest Territories Mineral Development Subsidiary Agreement. *Geol. Surv. Can. Open File Rep.* **1992**, *2484*, 279–284. [CrossRef]
10. Bleeker, W.; Ketchum, J.W.F.; Jackson, V.A.; Villeneuve, M.E. The Central Slave Basement Complex: Part I. Its Structural Topology and Autochthonous Cover. *Can. J. Earth Sci.* **1999**, *36*, 1083–1109. [CrossRef]
11. Davis, W.J.; Canil, D.; Mackenzie, J.M.; Carbno, G.B. Petrology and U–Pb geochronology of lower crustal xenoliths and the development of a craton, Slave Province, Canada. *Lithos* **2003**, *71*, 541–573. [CrossRef]
12. Bleeker, W.; Ketchum, J.W.F.; Davis, W.J. The Central Slave Basement Complex: Part II. Age and tectonic significance of high-strain zones along the basement-cover contact. *Can. J. Earth Sci.* **1999**, *36*, 1111–1130. [CrossRef]
13. Davis, W.J.; Bleeker, W. Timing of plutonism, deformation, and metamorphism in the Yellowknife domain, Slave province, Canada. *Can. J. Earth Sci.* **1999**, *36*, 1169–1187. [CrossRef]
14. Davis, W.J.; Kjarsgaard, B.A. A Rb-Sr isochron age for a kimberlite from the recently discovered Lac De Gras Field, Slave Province, Northwest Canada. *J. Geol.* **1997**, *105*, 503–510. [CrossRef]
15. Masun, K.M.; Doyle, B.J.; Ball, S.; Walker, S. The geology and mineralogy of the Anuri kimberlite, Nunavut, Canada. *Lithos* **2004**, *76*, 75–97. [CrossRef]
16. Kretschmar, U. *Drybones Bay Kimberlite: Summary and Exploration Update; Exploration Overview 1996*; Northwest Territories Mining, Exploration and Geological Investigations, NWT Geological Mapping Division: Yellowknife, NT, Canada, 1996; pp. 3.27–23.28.
17. Kretschmar, U. *Drybones Bay Kimberlite: 1995 Spring Drill Report*; Open File 83627; NWT Geological Survey: Yellowknife, NT, Canada, 1995; pp. 1–50.
18. Power, M.A. Seismic signature of the Drybones Bay kimberlite pipe, N.W.T. *CIM Bull.* **1998**, *91*, 66–69.
19. Field, M.; Scott Smith, B.H. Contrasting geology and near-surface emplacement of kimberlite pipes in Southern Africa and Canada. In Proceedings of the 7th International Kimberlite Conference, Cape Town, South Africa, 11–17 April 1998; pp. 217–231.

20. Scott Smith, B.H. Canadian kimberlites: Geological characteristics relevant to emplacement. *J. Volcanol. Geotherm. Res.* **2008**, *174*, 9–19. [CrossRef]
21. Timmins, W.G. Report on the Drybones Bay property. Unpublished report, 2002; pp. 1–24.
22. Bird, H. Yellowknives Dene lose Drybones Bay exploration appeal. *CBC News*, 26 June 2015. Available online: https://www.cbc.ca/news/canada/north/yellowknives-dene-lose-drybones-bay-diamond-exploration-appeal-1.3128489 (accessed on 24 October 2018).
23. Norman, M.D.; Pearson, N.J.; Sharma, A.; Griffin, W.L. Quantitative analysis of trace elements in geological materials by laser ablation ICPMS: Instrumental operating conditions and calibration values of NIST glasses. *J. Geostand. Geoanal. Res.* **1996**, *20*, 247–261. [CrossRef]
24. Jackson, S.E.; Pearson, N.J.; Griffin, W.L.; Belousova, E.A. The application of laser ablation-inductively coupled plasma-mass spectrometry to in situ U–Pb zircon geochronology. *Chem. Geol.* **2004**, *211*, 47–69. [CrossRef]
25. Paces, J.B.; Miller, J.D. Precise U–Pb ages of Duluth Complex and related mafic intrusions, northeastern Minnesota: Geochronological insights into physical, petrogenetic, paleomagnetic and tectonomagmatic processes associated with the 1.1 Ga midcontinent rift system. *J. Geophys. Res.* **1993**, *98*, 13997–14013. [CrossRef]
26. Petrus, J.A.; Kamber, B.S. VizualAge: A novel approach to laser ablation ICPMS U–Pb geochronology data reduction. *J. Geostand. Geoanal. Res.* **2012**, *36*, 247–270. [CrossRef]
27. Woodhead, J.D.; Hellstrom, J.; Hergt, J.; Grieg, A.; Maas, R. Isotopic and elemental imaging of geological materials by laser ablation Inductively Coupled Plasma mass spectrometry. *J. Geostand. Geoanal. Res.* **2007**, *31*, 331–343. [CrossRef]
28. Ludwig, K.R. Isoplot 3.75. A Geochronological Toolkit for Microsoft Excel 2012, Berkeley Geochronology Center Special Publication No. 5. Available online: http://www.bgc.org/isoplot_etc/isoplot/Isoplot3_75-4_15manual.pdf (accessed on 27 September 2018).
29. Lyakhovich, V.V. Zircons in diamond-bearing rocks. *Trans. Russ. Acad. Sci. Earth Sci. Sect.* **1996**, *347*, 179–199.
30. Belousova, E.A.; Griffin, W.L.; Pearson, N.J. Trace element composition and cathodoluminescence properties of southern African kimberlitic zircons. *Min. Mag.* **1998**, *62*, 355–366. [CrossRef]
31. Page, F.Z.; Fu, B.; Kita, N.T.; Fournelle, J.; Spicuzza, M.j.; Schulze, D.J.; Viljoen, F.; Basei, M.A.S.; Valley, J.W. Zircons from kimberlite: New insights from oxygen isotopes, trace elements, and Ti in zircon thermometry. *Geochim. Cosmochim. Acta* **2007**, *71*, 3887–3903. [CrossRef]
32. Belousova, E.A.; Griffin, W.L.; O'Reilly, S.Y.; Fisher, N.I. Igneous zircon: Trace element composition as an indicator of source rock type. *Contrib. Mineral. Petrol.* **2002**, *143*, 602–622. [CrossRef]
33. Kelly, C.J.; Schneider, D.A.; Lajoie, M.-È.; Jackson, S.E.; McFarlane, C.R. U–Pb geochronology and trace element composition of zircon from the Horseshoe Lake greenstone belt, Superior Province, Canada: Implications for the tectonic and metamorphic history. *Can. J. Earth Sci.* **2018**, *55*, 172–187. [CrossRef]
34. Grimes, C.B.; Wooden, J.L.; Cheadle, M.J.; John, B.E. "Fingerprinting" tectono-magmatic provenance using trace elements in igneous zircon. *Contrib. Miner. Petrol.* **2015**, *170*, 46. [CrossRef]
35. Hanchar, J.M.; Van Westrenen, W. Rare Earth Element Behaviour in Zircon-Melt Systems. *Elements* **2007**, *3*, 37–42. [CrossRef]
36. Li, H.-Y.; Chen, R.-X.; Zheng, Y.-F.; Hu, Z. The crust-mantle interaction in continental subduction channels: Zircon evidence from orogenic peridotite in the Sulu orogen. *J. Geophys. Res. Solid Earth* **2016**, *121*, 687–712. [CrossRef]
37. Watson, E.B.; Wark, D.A.; Thomas, J.B. Crystallization thermometers for zircon and rutile. *Contrib. Miner. Petrol.* **2006**, *151*, 413–433. [CrossRef]
38. Simonetti, A.; Neal, C.R. In-situ chemical, U–Pb dating, and Hf isotope investigation of megacrystic zircons, Malaita (Solomon Islands): Evidence for multi-stage alkaline magmatic activity beneath the Ontong Java Plateau. *Earth Planet Sci. Lett.* **2010**, *295*, 251–261. [CrossRef]
39. Sutherland, L.; Graham, I.; Yaxley, G.; Armstrong, R.; Giuliani, G.; Hoskin, P.; Nechaev, V.; Woodhead, J. Major zircon megacryst suites of the Indo-Pacific lithospheric margin (ZIP) and their petrogenetic and regional implications. *Miner. Petrol.* **2016**, *110*, 399–420. [CrossRef]
40. Hinton, R.W.; Upton, B.G.J. The chemistry of zircon: Variations within and between large crystals from syenite and alkali basalt xenoliths. *Geochim. Cosmochim. Acta* **1991**, *55*, 3287–3302. [CrossRef]

41. Berryman, A.K.; Stiefenhoffer, J.; Shee, S.R.; Wyatti, B.A.; Belousova, E.A. The discovery and geology of the Timber Creek kimberlites, Northern Territory, Australia. In Proceedings of the 7th International Kimberlite Conference, Cape Town, South Africa, 11–17 April 1998; Gurney, J.J., Dawson, B., Nixon, P.H., Eds.; Red Roof Design: Cape Town, South Africa, 1999; pp. 30–39.
42. Visonà, D.; Caironi, V.; Carraro, A.; Dallai, L.; Fioretti, A.M.; Fanning, M. Zircon megacrysts from basalts of the Venetian Volcanic Province (NE Italy): U–Pb ages, oxygen isotopes and REE data. *Lithos* **2007**, *94*, 168–180. [CrossRef]
43. Yu, Y.; Xu, X.; Chen, X. Genesis of zircon megacrysts in Cenozoic alkali basalts and the heterogeneity of subcontinental lithospheric mantle, eastern China. *Miner. Petrol.* **2010**, *100*, 75–94. [CrossRef]
44. Cong, F.; Li, S.-Q.; Lin, F.-C.; Shi, M.F.; Zhu, H.-P.; Siebel, W.; Chen, F. Origin of zircon megacrysts from cenozoic basalts in northeastern Cambodia: Evidence from U-Pb age, Hf-O isotopes, and inclusions. *J. Geol.* **2016**, *126*, 221–234. [CrossRef]
45. Dawson, J.B.; Hill, P.G.; Kinny, P.D. Mineral chemistry of a zircon-bearing, composite, veined and metasomatized upper-mantle peridotite xenolith from kimberlite. *Contrib. Miner. Petrol.* **2001**, *140*, 720–733. [CrossRef]
46. McDonough, W.F.; Sun, S.-S. The composition of the Earth. *Chem. Geol.* **1995**, *120*, 223–253. [CrossRef]
47. Palme, H.; O'Neill, H.S.C. Cosmochemical estimates of mantle composition. In *Treatise on Geochemistry*; Carlson, R.W., Holland, H.D., Turekian, K.K., Eds.; Elsevier: Amsterdam, The Netherlands, 2003; Volume 2, pp. 1–38. [CrossRef]
48. Pearson, D.G.; Canil, D.; Shirey, S.B. Mantle Samples Included in Volcanic Rocks: Xenoliths and Diamonds. In *Treatise on Geochemistry*; Carlson, R.W., Holland, H.D., Turekian, K.K., Eds.; Elsevier: Amsterdam, The Netherlands, 2003; Volume 2, pp. 171–275. [CrossRef]
49. Zheng, J.; Griffin, W.L.; O'Reilly, S.Y.; Zhang, M.; Pearson, N. Zircons in mantle xenoliths record the Triassic Yangtze–North China continental collision. *Earth Planet. Sci. Lett.* **2006**, *247*, 130–142. [CrossRef]
50. Chakhmouradian, A.R.; Reguir, E.P.; Kamenetsky, V.S.; Sharygin, V.V.; Golovin, A.V. Trace-element partitioning in perovskite: Implications for the geochemistry of kimberlites and other mantle-derived undersaturated rocks. *Chem. Geol.* **2013**, *253*, 112–131. [CrossRef]
51. Daniela Rubatto, D.; Hermann, J. Experimental zircon/melt and zircon/garnet trace element partitioning and implications for the geochronology of crustal rocks. *Chem. Geol.* **2007**, *241*, 38–61. [CrossRef]
52. Burnham, A.D.; Berry, A.J. An experimental study of trace element partitioning between zircon and melt as a function of oxygen fugacity. *Geochim. Cosmochim. Acta* **2012**, *95*, 196–212. [CrossRef]
53. Hoffman, J.F.; Long, J.V.P. Unusual sector zoning in Lewisian zircons. *Min. Mag.* **1984**, *48*, 513–517. [CrossRef]